Quantum-interference transport through surface layers of indium-doped ZnO nanowires

2013 Nanotechnology 24 245203

(http://iopscience.iop.org/0957-4484/24/24/245203)

Nanotechnology **24** (2013) 245203 (14pp) doi:10.1088/0957-4484/24/24/245203

Quantum-interference transport through surface layers of indium-doped ZnO nanowires

Shao-Pin Chiu[1], **Jia Grace Lu**[2] **and Juhn-Jong Lin**[1,3]

[1] NCTU-RIKEN Joint Research Laboratory and Institute of Physics, National Chiao Tung University, Hsinchu 30010, Taiwan
[2] Department of Physics and Astronomy, University of Southern California, Los Angeles, CA 90089-0484, USA
[3] Department of Electrophysics, National Chiao Tung University, Hsinchu 30010, Taiwan

E-mail: jjlin@mail.nctu.edu.tw

Received 7 January 2013, in final form 27 April 2013
Published 20 May 2013
Online at stacks.iop.org/Nano/24/245203

Abstract

We have fabricated indium-doped ZnO (IZO) nanowires (NWs) and carried out four-probe electrical-transport measurements on two individual NWs with geometric diameters of ≈70 and ≈90 nm in a wide temperature T interval of 1–70 K. The NWs reveal overall charge conduction behavior characteristic of disordered metals. In addition to the T dependence of resistance R, we have measured the magnetoresistance (MR) in magnetic fields applied either perpendicular or parallel to the NW axis. Our $R(T)$ and MR data in different T intervals are consistent with the theoretical predictions of the one- (1D), two- (2D) or three-dimensional (3D) weak-localization (WL) and the electron–electron interaction (EEI) effects. In particular, a few dimensionality crossovers in the two effects are observed. These crossover phenomena are consistent with the model of a 'core–shell-like structure' in individual IZO NWs, where an outer shell of thickness t ($\simeq$15–17 nm) is responsible for the quantum-interference transport. In the WL effect, as the electron dephasing length L_φ gradually decreases with increasing T from the lowest measurement temperatures, a 1D-to-2D dimensionality crossover takes place around a characteristic temperature where L_φ approximately equals d, an effective NW diameter which is slightly smaller than the geometric diameter. As T further increases, a 2D-to-3D dimensionality crossover occurs around another characteristic temperature where L_φ approximately equals t ($<d$). In the EEI effect, a 2D-to-3D dimensionality crossover takes place when the thermal diffusion length L_T progressively decreases with increasing T and approaches t. However, a crossover to the 1D EEI effect is not seen because $L_T < d$ even at $T = 1$ K in our IZO NWs. Furthermore, we explain the various inelastic electron scattering processes which govern L_φ. This work demonstrates the complex and rich nature of the charge conduction properties of group-III metal-doped ZnO NWs. This work also strongly indicates that the surface-related conduction processes are essential to doped semiconductor nanostructures.

(Some figures may appear in colour only in the online journal)

1. Introduction

In recent years, nanometer-scale structures have opened up numerous new horizons in both fundamental and applied research [1]. Among the various forms of nanoscale structures, nanowires (NWs) provide unique advantages for facilitating four-probe electrical-transport measurements over a wide range of temperature T and in externally applied magnetic fields B. In-depth investigations of the rich phenomena and the underlying physics of intrinsic

charge and spin conduction processes in single NWs are thus feasible. Indeed, to date, significant advances have been made in studies of metallic [2–6], magnetic [7], semiconducting [8–16], and superconducting [17] NWs.

Zinc oxide (ZnO) NWs are probably the most extensively studied materials among all kinds of semiconductor NW, due to their intricate physical properties as well as their widespread potential applications in nanoelectronic and spintronic devices [18, 19]. In addition to the initial investigations of natively (unintentionally) doped samples, artificially doped ZnO NWs have attracted much attention. For instance, the n-type doping of Ga and In, among other metal atoms, into ZnO NWs has recently been explored [20, 21]. The electrical-transport properties of individual In-doped ZnO (hereafter referred to as IZO) NWs [22] and NW transistors [14] have also been reported. Despite the intense experimental studies in the past years, the electrical conduction mechanisms in the parent ZnO NWs have only been explained recently. Chiu *et al* [9] and Tsai *et al* [10] have demonstrated that most artificially synthesized ZnO NWs, essentially independent of the growth method, are moderately highly doped and weakly self-compensated, resulting in a splitting of the impurity band. As a result, the overall charge-transport behavior is due to the 'split-impurity-band conduction' processes. Furthermore, Chiu *et al* [9] and Tsai *et al* [10] have shown that many natively doped ZnO NWs, which inherently possess high carrier (electron) concentrations, lie on the insulating side of, but very close to, the metal–insulator (M–I) transition. Therefore, it is expected that incorporation of a few atomic per cent of, e.g., the group-III indium atoms into ZnO NWs may promote the NWs to fall on the metallic side of the M–I transition. (The group-III atoms, Al, Ga, and In, are shallow donors in ZnO [23].) Thus, the IZO NWs should reveal electrical conduction properties characteristic of disordered conductors. In particular, the quantum-interference weak-localization (WL) and the electron–electron interaction (EEI) effects should be manifest at low temperatures [24–26].

Apart from the interesting low-dimensional electrical-transport properties that could be expected for NW structures, ZnO NWs inherit some complexities, as compared with other NW materials. In particular, the question of whether the surfaces of a ZnO NW are more conducting or less conducting than the bulk has been investigated by several groups. It is now accepted that surface electron accumulation layers, band bending effects, compositional nonstoichiometries, ambient conditions, etc, can all markedly affect the electrical properties of a surface [27, 28]. Recent measurements of resistance R and magnetoresistance (MR) by Chiu *et al* [9], Hu *et al* [29], and Tsai *et al* [10] have revealed that surface conduction is particularly important in those ZnO NWs lying close to the M–I transition. In this context, it would be very interesting to investigate if surface conduction could also be pronounced in IZO NWs, which are even more metallic than the natively doped ZnO NWs. Indeed, in this work, we have measured and analyzed the T dependence of R as well as the B dependence of both perpendicular MR and parallel MR in two IZO NWs over a wide T interval of 1–70 K. We found a few dimensionality crossovers in the WL and the EEI effects as T gradually increases from 1 to 70 K. These results strongly point to dominating roles of the *surface-related conduction* processes, prompting us to propose a 'core–shell-like structure' in individual IZO NWs. This present work demonstrates the complex and rich nature of charge-transport processes in ZnO-based NWs. This work also illustrates that quantum-interference transport studies can provide a useful probe for the electron scattering processes in these nanoscale materials. Furthermore, regarding the materials and technological aspects, we would like to stress that the nature of impurity doping semiconductor nanostructures is *intrinsically distinct* from doping the bulks. The recent theoretical calculations of Dalpian and Chelikowsky [30] have shown that *dopants would be energetically in favor of segregating to the surfaces rather than distributing uniformly across the radial direction*. Their theory provides a strong microscopic support for our experimental observation of a core–shell-like structure in the IZO NWs.

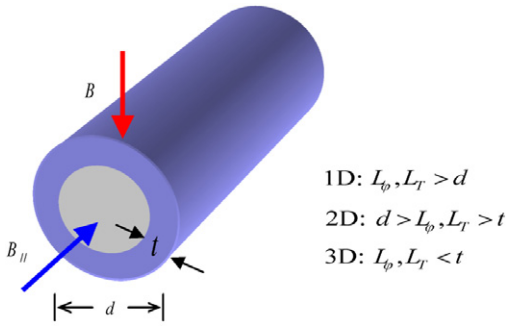

Figure 1. A schematic diagram for our proposed core–shell-like structure in IZO NWs. The blue outer shell of thickness t is responsible for the WL and the EEI transport. d is an effective diameter which differs slightly from the geometric diameter. The experimental conditions for the 1D, 2D, and 3D WL and EEI effects are summarized on the right.

For the convenience of discussion, we first present our model of the core–shell-like structure and summarize the main results of this work. Figure 1 shows a schematic diagram of the core–shell-like structure with a surface conduction layer of thickness t ($\simeq$15–17 nm in our IZO NWs). The sizes of the effective NW diameter d and the thickness t, relative to the electron dephasing length L_φ and the thermal diffusion length L_T, determine the observed one-dimensional (1D), two-dimensional (2D), or three-dimensional (3D) WL and EEI effects, as summarized in figure 1. The dephasing length $L_\varphi = \sqrt{D\tau_\varphi}$ is the characteristic length scale in the single-particle WL effect and the thermal length $L_T = \sqrt{D\hbar/k_B T}$ is the characteristic length scale in the many-body EEI effect, where D is the diffusion constant, τ_φ is the electron dephasing time, $2\pi\hbar$ is the Planck constant, and k_B is the Boltzmann constant. Table 1 summarizes the various T intervals over which different dimensionalities in the WL and the EEI effects are observed in our IZO NWs.

This paper is organized as follows. In section 2, we discuss our experimental method for the NW synthesis and characterizations as well as the low-T four-probe resistance

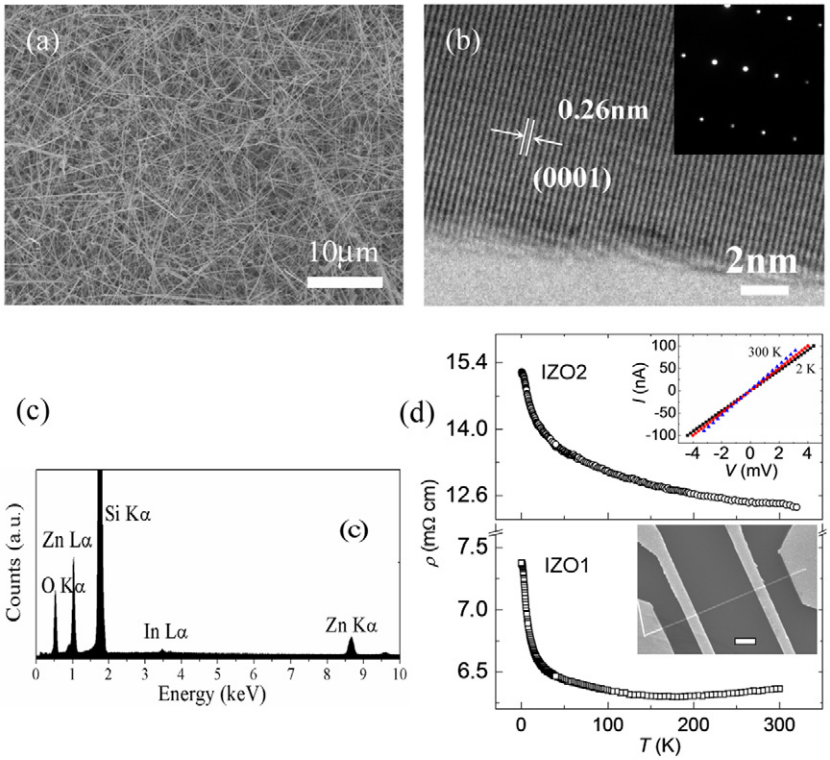

Figure 2. (a) An SEM image of as-grown IZO NWs on a tin-coated Si substrate. (b) An HRTEM image of a single IZO NW. The inset shows the corresponding selected-area electron diffraction pattern. (c) EDX spectrum of as-grown IZO NWs. (d) Resistivity ρ as a function of temperature for the IZO1 and IZO2 NWs, as indicated. The inset in the upper panel shows the I–V curves for the IZO2 NW at 2, 40 and 300 K. Note that these I–V curves are linear. They nearly overlap because the resistivity of this given NW depends weakly on T (main panel). The inset in the lower panel shows an SEM image of the IZO1 NW device. The scale bar is 1 μm.

Table 1. Summary of approximate temperature intervals over which different dimensionalities in the WL and the EEI effects are observed in IZO NWs.

	WL effect			EEI effect		
Nanowire	1D	2D	3D	1D	2D	3D
IZO1	∼1–7 K	∼7–50 K	$\gtrsim$50 K	—	∼3–11 K	$\gtrsim$14 K
IZO2	—	∼1–40 K	$\gtrsim$40 K	—	—	$\gtrsim$3 K

and MR measurements. In sections 3–5, we present our experimental results and discussions in great detail. We carry out analyses of the perpendicular MR data and the parallel MR data (section 3) as well as the T dependence of R (section 4) to illustrate how a conducting outer layer must exist in single IZO NWs. As a consequence, a few 1D-to-2D and 2D-to-3D dimensionality crossovers in the WL and the EEI effects are observed. In section 5, we identify the underlying electron dephasing processes. Our conclusion is given in section 6.

2. Experimental method

Our IZO NWs were synthesized by the laser-assisted chemical vapor deposition (CVD) method, as described previously [22]. The scanning electron microscopy (SEM) image in figure 2(a) shows that IZO NWs with diameters ranging roughly from 40 to 100 nm were formed on a tin-coated Si substrate. The high-resolution transmission electron microscopy (HRTEM) image and selected-area electron diffraction pattern in figure 2(b) indicate that In atoms were effectively incorporated into the wurtzite crystal lattice of ZnO and the single-crystalline structure with the (0001) growth direction was maintained. The energy-dispersive x-ray (EDX) spectrum displayed in figure 2(c) indicates an In to Zn atomic ratio of approximately 3 at.%, suggesting successful incorporation of In atoms into the ZnO crystal lattice. The NW growth and doping method as well as the structural and composition analyses have been previously discussed in [22].

We have fabricated several single IZO NW devices with the four-probe configuration by utilizing the electron-beam lithography technique. The devices reported in this paper were taken from the same batch of NWs. Submicron Cr/Au (10/100 nm) electrodes were made via thermal evaporation deposition. The inset of the lower panel in figure 2(d) shows an SEM image of the IZO1 NW device. The contact resistance between an electrode and the NW is typically a few kiloohms

Table 2. Relevant parameters of two single IZO NW devices. dia is the geometric diameter measured by SEM, L is the length between the two voltage leads in a four-probe configuration, ρ is the resistivity, n is the carrier concentration, E_F (k_F) is the Fermi energy (wavenumber), ℓ (τ_e) is the elastic mean-free path (time), and D is the diffusion constant. ℓ, τ_e, D, and $k_F\ell$ values are for 10 K.

Nanowire	dia (nm)	L (μm)	R(300 K) (kΩ)	ρ(300 K) (mΩ cm)	ρ(10 K) (mΩ cm)	n (cm^{-3})	E_F (meV)	ℓ (nm)	τ_e (fs)	D (cm^2 s^{-1})	$k_F\ell$
IZO1	68	3.8	66.6	6.4	6.7	1.7×10^{19}	100	2.8	7.3	3.6	2.2
IZO2	92	1.9	35.5	12	15	6.8×10^{18}	55	2.4	8.4	2.2	1.4

at 300 K and ~20 kΩ at 4 K. Extensive measurements of the resistances and magnetoresistances have been carried out on two devices. The experimental setup and measurement procedures were similar to those employed in our previous studies of single natively doped ZnO NWs [9, 10] and indium tin oxide (ITO) NWs [5]. The $R(T)$ and MR curves were measured by utilizing a Keithley K-220 or K-6430 as a current source and a high-impedance (TΩ) Keithley K-2635A or K-6430 as a voltameter. The resistances reported in this work were all measured by scanning the current–voltage (I–V) curves at various fixed T values between 300 and 1 K. The resistance at a given T value was then determined from the region around the zero bias voltage, where the I–V curve was definitely linear; see the inset in the upper panel of figure 2(d). In fact, since our IZO NWs had relatively low resistivities (~10 mΩ cm), which depended very weakly on T in the wide temperature range 1–300 K, the NWs were 'metallic-like' and the electron-beam lithographic contacts were already Ohmic without any heat treatment. Electron overheating at our lowest measurement temperatures was carefully monitored and largely avoided, except that there might be slight heating for those data points taken at $T = 1$ K. This possible slight electron heating at 1 K will not affect any of our discussions or conclusion, except that the extracted value of τ_φ^{-1} (1 K) might be slightly overestimated (figure 7). Notice that, since we had employed the four-probe configuration, the measured resistances (resistivities) were thus the intrinsic resistances (resistivities) of the individual NWs. The relevant parameters of the two individual IZO NW devices studied in this work are listed in table 2.

3. Results and discussion: magnetoresistance in the weak-localization effect

This section is divided into three. In section 3.1, we present our estimates of the electronic parameters in our IZO NWs. In section 3.2, we present our perpendicular MR data and the observed dimensionality crossovers in the WL effect. In section 3.3, we analyze our parallel MR data to further determine and confirm the thickness of the outer conduction shell in single IZO NWs.

3.1. Estimate of nanowire electronic parameters

In order to facilitate quantitative comparison of our $R(T)$ and MR data with the WL and the EEI theoretical predictions, we first discuss the estimates of the relevant electronic parameters of our IZO NWs. The carrier concentration n of a doped semiconductor NW cannot be readily measured, e.g., by using the conventional Hall effect, due to the small transverse dimensions of a single NW. Fortunately, insofar as single-crystalline ZnO materials (films and bulks) are concerned, an empirical relation between the room-temperature resistivity ρ(300 K) and n has been comprehensively compiled and reliably established by Ellmer in figure 4 of [31]. Furthermore, Chiu *et al* [9] and Tsai *et al* [10] have recently shown that this Ellmer ρ–n empirical relation can well be extended to the case of individual single-crystalline ZnO NWs. Therefore, in this study we have applied this empirical relation to evaluate the n values in our IZO NWs.

It is worth noting that the n values we evaluated (table 2) are in reasonable consistency with that extracted from direct measurements by using the back-gate method [22]. For example, in an IZO NW with ρ (4 K) = 2.7 mΩ cm, the back-gate method reported an estimate of $n \approx 1.2 \times 10^{20}$ cm^{-3}. Alternatively, according to the Ellmer ρ–n empirical relation [31], such a resistivity would imply a value of $n \approx 8 \times 10^{19}$ cm^{-3}. That is, the n values estimated according to the two independent methods agree to within a factor of ≈1.5. Since the critical carrier concentration for the M–I transition in single-crystalline ZnO occurs at $n_c \approx 5 \times 10^{18}$ cm^{-3} [9, 10, 32], our doped IZO NWs obviously lie on the metallic side of, but close to, the M–I transition. That our NWs lie close to the M–I transition boundary is directly evident in the fact that our measured T dependence of ρ is weak, namely, $\rho(1\text{ K})/\rho(300\text{ K}) \lesssim 1.2$ in both NWs (figure 2(d)). In the IZO1 NW, ρ decreases with reducing T between 180 and 300 K, before it increases with further decrease in T. The metallic-like behavior results from the incorporation of a few atomic per cent of In atoms (donors) into the ZnO NW crystal lattice as well as from the In doping induced oxygen vacancies [20]. The notable resistivity rise below ~40 K originates from the WL and the EEI effects. Numerically, the ρ(300 K) values of the IZO1 and IZO2 NWs are approximately one order of magnitude lower than those of the natively doped ZnO NWs that we had previously studied [9, 10]. Moreover, these ρ(300 K) values are ~3 orders of magnitude lower than that in a two-probe individual IZO NW transistor recently fabricated by Xu *et al* [14].

In estimating the other charge carrier parameters which are listed in table 2, we have assumed a free-electron model and taken an effective electron mass of $m^* = 0.24\,m$ in the conduction band [33], where m is the free-electron mass. We obtain the electron mobility μ(300 K) ≈55 cm^2 V^{-1} s^{-1} in the IZO1 NW and 75 cm^2 V^{-1} s^{-1} in the IZO2 NW. These values are slightly lower than that (~100 cm^2 V^{-1} s^{-1}) found

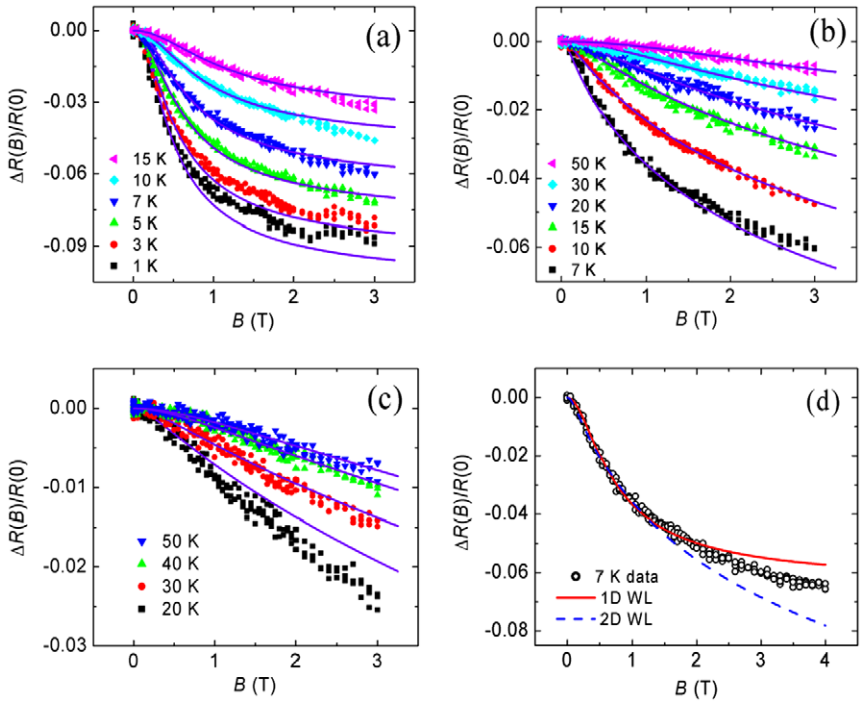

Figure 3. Normalized MR, $\Delta R(B)/R(0) = (R(B) - R(0))/R(0)$, as a function of perpendicular magnetic field of the IZO1 NW in different T regions, as indicated. The symbols are the experimental data and the solid curves are the theoretical predictions of the (a) 1D (equation (1)), (b) 2D (equation (3)), and (c) 3D (equation (2)) WL effects. (d) $\Delta R(B)/R(0)$ at 7 K with the theoretical predictions of the 1D and 2D WL effects, as indicated.

in natively doped ZnO NWs [9]. Note that our evaluated Fermi energies E_F are 100 and 55 meV in the IZO1 and IZO2 NWs, respectively. These values are larger than the thermal energy $k_B T$ at 300 K, and also larger than the major shallow donor level (∼30 meV below the conduction band minimum [9, 10, 34]) in the parent ZnO. Therefore, degenerate Fermi-liquid and metallic behavior is to be expected in our NWs. As a consequence, all of our electronic parameters depend only weakly on T, as compared with those in typical semiconductor NWs that exhibit, e.g., hopping conduction processes[4].

3.2. Perpendicular magnetoresistance in the weak-localization effect

In disordered conductors and at low temperatures, the WL and the EEI effects cause pronounced quantum-interference transport phenomena which depend sensitively on T and B. The WL effect results from the constructive interference between a pair of time-reversal partial electron waves which traverse a closed trajectory in a random potential. The time-reversal symmetry will be readily broken in the presence of a small B field [24, 25]. The low-field MR can provide quantitative information on the various electron dephasing mechanisms, such as the inelastic electron–electron scattering, electron–phonon scattering, spin–orbit scattering, and magnetic spin–spin scattering [35]. The WL effects in different dimensionalities assume different functional forms of MR [24–26]. Therefore, it is of crucial importance to apply the appropriate MR expressions to describe the WL effect in those samples (e.g., NWs and thin films) whose transverse dimensions are comparable to the dephasing length L_φ. In such cases, a dimensionality crossover of the WL effect is deemed to occur if the measurement T is varied sufficiently widely [36]. Moreover, an external B applied in the perpendicular or the parallel orientation relative to the current flow can result in distinct MR, because the WL effect is an orbital phenomenon in nature. Similarly, dimensionality crossovers could occur in the EEI effect (section 4).

Figures 3(a)–(d) show the normalized MR, $\Delta R(B)/R(0) = (R(B) - R(0))/R(0)$, of the IZO1 NW as a function of perpendicular magnetic field in several T regions, as indicated. (The B fields were applied perpendicular to the NW axis.) The symbols are the experimental data and the solid curves are the WL theoretical predictions for 1D (figure 3(a)), 2D (figure 3(b)), and 3D (figure 3(c)), respectively. Figure 3(d) shows a plot of the measured perpendicular MR at 7 K together with both the 1D and the 2D WL theoretical predictions, as indicated. We notice that in all figures 3(a)–(d) the MR data are negative, suggesting that the spin–orbit (s–o) scattering rate is relatively weak compared with the inelastic electron scattering rate at all T down to 1 K. In other words, the s–o scattering length $L_{so} = \sqrt{D\tau_{so}}$ is always longer than L_φ, where τ_{so} is the s–o scattering time. This observation of

[4] In the evaluation of ρ in a given IZO NW, we have assumed that the electrical current passes through the whole volume of an NW. If the electrical conduction is not through the bulk of an NW, the above estimate of ρ will be changed by an amount of $\lesssim$50%, according to the geometries of our core–shell-like structure. Since $k_F \propto n^{1/3}$, the values of the other electronic parameters will thus be modified by smaller amounts of $\lesssim$15%. Such modifications will not affect any conclusions drawn in this work.

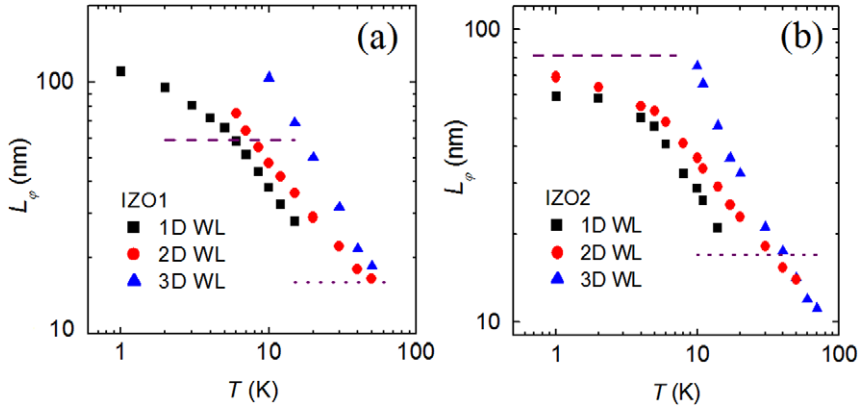

Figure 4. Electron dephasing length L_φ as a function of temperature for the (a) IZO1 and (b) IZO2 NWs. Different symbols represent the L_φ values extracted according to different dimensional WL MR expressions: 1D equation (1) (squares), 2D equation (3) (circles), and 3D equation (2) (triangles). The dashed (dotted) line indicates the effective NW diameter d (the outer conduction shell thickness t).

a very weak s–o scattering is consistent with the conclusion recently drawn from the WL studies of metallic-like ZnO NWs [9] and ZnO nanoplates [37, 38]. Microscopically, the comparatively weak s–o coupling in ZnO is thought to originate from the small energy splitting at the top of the valence band [39]. A doping of ≈3 at.% of moderately heavy In atoms in this work does not induce any appreciable enhancement of the s–o coupling.

The MR due to the 1D WL effect in the presence of an external B applied either perpendicular or parallel to the NW axis is given by [40, 41], in terms of the normalized resistance $\Delta R(B)/R(0) = (R(B) - R(0))/R(0)$,

$$\frac{\Delta R(B)}{R(0)} = \frac{e^2}{\pi\hbar}\frac{R}{L}\left\{\frac{3}{2}\left[\left(\frac{1}{L_\varphi^2}+\frac{4}{3L_{\rm so}^2}+\frac{1}{D\tau_{\rm B}}\right)^{-1/2} - \left(\frac{1}{L_\varphi^2}+\frac{4}{3L_{\rm so}^2}\right)^{-1/2}\right] - \frac{1}{2}\left[\left(\frac{1}{L_\varphi^2}+\frac{1}{D\tau_{\rm B}}\right)^{-1/2} - L_\varphi\right]\right\}, \quad (1)$$

where R is the resistance of a quasi-1D NW of length L, and the characteristic time scale $\tau_{\rm B}$ represents the dephasing ability of the B field. The form of $\tau_{\rm B}$ depends on the orientation of B relative to the current flow and the shape of the NW [40]. There are two situations which have been explicitly theoretically calculated. First, for an NW with a square cross section and side a in B applied perpendicular to the NW axis, $\tau_{\rm B} = 3L_{\rm B}^4/(Da^2)$, where the magnetic length $L_{\rm B} = \sqrt{\hbar/eB}$. Second, for an NW with a circular cross section and diameter d in B applied parallel to the NW axis, $\tau_{\rm B} = 8L_{\rm B}^4/(Dd^2)$. In practice, both side a and diameter d can be treated as adjustable parameters, because the effective cross-sectional area responsible for the charge conduction may differ from the geometric cross-sectional area of the given NW under study. In other words, the NW may be inhomogeneous (e.g., due to O vacancies, surface absorption/desorption, variations in compositions, surface states [42], accumulation layers [43, 44], etc) and the electrical conduction is not through the whole volume of the NW [27, 29].

In plotting figure 3(a), we have used equation (1) and rewritten $\tau_{\rm B} = 3L_{\rm B}^4/(Da^2) \equiv 12L_{\rm B}^4/(D\pi d^2)$ to least-squares fit the measured MR data for $B < 0.5$ T, and then generated the theoretical curves for a B range up to 3.25 T. (We have treated $\tau_{\rm B}$, and thus d, as an adjustable parameter.) Numerically, we obtained T-independent (average) values of $d \simeq 59$ nm and $L_{\rm so} \simeq 140$ nm for all the MR curves plotted in figure 3(a). The only T-dependent adjustable parameter is L_φ, which is plotted in figure 4(a) as a function of T. Figure 4(a) shows that L_φ (the squares) decreases from 110 nm at 1 K to 28 nm at 15 K. It should be noted that our extracted L_φ value becomes shorter than the effective NW diameter d as T increases to above ∼7 K. Such a result is not self-consistent and it violates the applicability of equation (1). That is, under such circumstances, one should consider a possible dimensionality crossover to the 3D WL effect at $T > 7$ K. A similar observation has recently been pointed out by Hsu *et al* [5] in their WL studies of single ITO NWs. In any case, one should be cautious about the validity of the extracted L_φ values in this moderately high T region.

To examine whether a crossover from the 1D to the 3D WL effect takes place in the IZO1 NW at $T > 7$ K, we now compare our MR data with the 3D WL theoretical predictions. The 3D WL MR is given by [35, 45, 46], in terms of normalized magnetoresistivity $\Delta\rho(B)/\rho^2(0) = (\rho(B) - \rho(0))/\rho^2(0)$,

$$\frac{\Delta\rho(B)}{\rho^2(0)} = \frac{e^2}{2\pi^2\hbar}\sqrt{\frac{eB}{\hbar}}\left\{\frac{1}{2\sqrt{1-\gamma}}\left[f_3\left(\frac{B}{B_-}\right) - f_3\left(\frac{B}{B_+}\right)\right] - f_3\left(\frac{B}{B_2}\right) - \sqrt{\frac{4B_{\rm so}}{3B}} \times\left[\frac{1}{\sqrt{1-\gamma}}\left(\sqrt{t_+}-\sqrt{t_-}\right)+\sqrt{t}-\sqrt{t+1}\right]\right\}, \quad (2)$$

where

$$\gamma = \left[\frac{3g^*\mu_{\rm B}B}{4eD(2B_{\rm so}-B_0)}\right]^2,$$

$$t = \frac{3B_\varphi}{2(2B_{\rm so}-B_0)}, \qquad t_\pm = t + \frac{1}{2}(1 \pm \sqrt{1-\gamma}),$$

$$B_\varphi = B_{\rm in} + B_0, \qquad B_2 = B_{\rm in} + \tfrac{1}{3}B_0 + \tfrac{4}{3}B_{\rm so},$$

$$B_\pm = B_\varphi + \tfrac{1}{3}(2B_{\rm so} - B_0)(1 \pm \sqrt{1-\gamma}),$$

g^* ($= -1.93$ in the ZnO material [47]) is the electron Landé g factor, μ_B is the Bohr magneton, and

$$f_3(z) \approx 2\left(\sqrt{2+\frac{1}{z}}-\sqrt{\frac{1}{z}}\right) - \left[\left(\frac{1}{2}+\frac{1}{z}\right)^{-1/2}+\left(\frac{3}{2}+\frac{1}{z}\right)^{-1/2}\right]+\frac{1}{48}\left(2.03+\frac{1}{z}\right)^{-3/2}.$$

Here the characteristic fields are connected with the electron scattering times through the relation $B_j = \hbar/(4eD\tau_j)$, with the subscript j standing for φ (the dephasing field/time), in (the inelastic scattering field/time), so (the s–o scattering field/time), 0 (the 'saturated' scattering field/time as $T \to 0$ K), and e (the elastic scattering field/time). (B_e will be used in equation (3).) The function f_3 is an infinite series, which can be approximately expressed as above, which is known to be accurate to be better than 0.1% for all arguments z [48].

Figure 3(c) shows the normalized MR and the least-squares fits to the theoretical predictions of equation (2) at four T values between 20 and 50 K. This figure reveals that, as T increases to above ~20 K, the theoretical curves can reasonably describe the experimental data. The L_φ values (triangles) thus extracted are plotted in figure 4(a). We obtain $L_\varphi = 50$ nm at 20 K and 19 nm at 50 K. Although our measured MR data at $T > 20$ K can seemingly be described by the 3D WL theory, we should stress that the agreement between the theory and the experiment is superficial. For instance, the inferred L_φ values (triangles) do not extrapolate to those L_φ values (squares) inferred from the low-T 1D regime. Furthermore, the extracted L_φ value would suggest a 3D-to-1D dimensionality crossover taking place at a relatively high T ~20 K, which is very unlikely. (Recall that the least-squares fits to the 1D MR theory do not lead to self-consistent results for $T \gtrsim 7$ K.) In fact, as we will demonstrate below, the charge carriers in our IZO NWs do not flow through the whole volume of the individual NWs. Instead, there is an outer conduction shell of thickness t in individual IZO NWs (figure 1), which is responsible for our observed quantum-interference electron conduction. Thus, at sufficiently low T where $L_\varphi \gtrsim d$, the electrical transport would be 1D with regard to the WL effect. On the other hand, at not too low T where $L_\varphi \lesssim d$, the low-field MR manifests the 2D WL effect. Note that, recently, *surface-related electrical conduction processes* have also been found in natively doped ZnO NWs which lie on the metallic side of, but close to, the M–I transition [9].

We now analyze our MR data at $T \gtrsim 7$ K in terms of the 2D WL theory. The MR due to the 2D WL effect in the presence of a perpendicular B field is given by [24, 49, 50], in terms of normalized sheet resistance $\Delta R_\square(B)/R_\square^2(0) = (R_\square(B) - R_\square(0))/R_\square^2(0)$,

$$\frac{\Delta R_\square(B)}{R_\square^2(0)} = \frac{e^2}{2\pi^2\hbar}\left[\Psi\left(\frac{1}{2}+\frac{B_1}{B}\right)-\frac{3}{2}\Psi\left(\frac{1}{2}+\frac{B_2}{B}\right) + \frac{1}{2}\Psi\left(\frac{1}{2}+\frac{B_\varphi}{B}\right)-\frac{1}{2}\ln\left(\frac{B_1^2 B_\varphi}{B_2^3}\right)\right], \quad (3)$$

where Ψ is the digamma function, and B_2 was defined below equation (2). B_1 is a characteristic field given by $B_1 = B_e + B_{so} + B_0/2 \simeq B_e$. In the least-squares fits of the predictions of equation (3) to our experimental MR data, we have treated the sheet resistance $R_\square = R/(L/w)$ as an adjustable parameter, where the resistance R and length L are directly measured, and w is defined as $w = \pi(\text{dia} - t)$, with dia being the geometric diameter of the NW determined via SEM (table 2). Thus, t is a fitting parameter. Note that we have approximated the outer conduction shell with a dodecagon in the fits to equation (3).[5]

Figure 3(b) shows the measured MR and the least-squares fits to equation (3) for the IZO1 NW at several T values between 7 and 50 K. This figure clearly indicates that the normalized MR in the low-field regime of $B \lesssim 1$ T can be well described by the theoretical predictions. Most important, the extracted L_φ values (circles) as a function of T are plotted in figure 4(a), and lie systematically below those extracted according to the 3D form of equation (2). Inspection of figure 4(a) indicates that the $L_\varphi(\gtrsim 7$ K) values inferred from the 2D WL theory, equation (3), *closely extrapolate to* those $L_\varphi(\lesssim 7$ K) values inferred from the 1D WL theory, equation (1). This observation is meaningful, and strongly suggests that the WL MR effect *smoothly crosses over* from the 1D regime to the 2D regime as T increases above ≈ 7 K. Indeed, we find that the measured MR data at 7 K and in $B \lesssim 1$ T can be reasonably well described by both equation (1) and equation (3) (figure 3(d)). Furthermore, it should be noted that, at this particular T value, the fitted dephasing length according to equation (3) is $L_\varphi(7\,\text{K}) \simeq 64$ nm. This is very close to the effective NW diameter d ($\simeq 59$ nm) inferred above from the 1D WL fits. Thus, the physical quantity d signifies the characteristic length scale that controls the dimensionality crossover between the 1D ($L_\varphi \gtrsim d$) and 2D ($L_\varphi \lesssim d$) WL regimes in the IZO1 NW.

If T continues to increase and L_φ gradually reduces, one would expect another possible dimensionality crossover from the 2D to the 3D WL effect. In fact, figures 3(b) and (c) together indicate that both equations (2) and (3) can describe the measured MR data at 50 K and in $B \lesssim 1.5$ T. The extracted $L_\varphi(50$ K) values according to both equations approach each other, being ≈15 nm (figure 4(a)). This result implies that a 2D-to-3D dimensionality crossover takes place around $T \sim 50$ K or slightly higher. In particular, the responsible length scale is ≈ 15 nm, which can be identified as the effective thickness t of the outer conduction shell. In short, in the

[5] Equation (3) was originally formulated for a planar structure and with the B field applied perpendicular to the film plane. In the present case, our conduction shell is roughly cylindrical. A similar situation occurred in multiwalled carbon nanotubes, where equation (3) had been successfully applied to describe the measured perpendicular MR in the 2D WL effect [51, 52]. In this work, directly applying this equation also gave satisfactory fitting results of L_φ and t for our IZO NWs. For example, we obtained $t \simeq 17 \pm 2$ nm for both NWs. Moreover, the fitted L_φ values differed by less than ≈10–15% from those plotted in figures 4(a) and (b). In a strict manner, for a cylindrical film, the normal to the surface component of the B field is not a constant but depends on the position of the surface component under consideration. In this case, the normal component of the applied B field, $B_\perp$, on each surface component has to be taken into account. In this work, we have approximated the cross-section of the conduction shell in our NWs with a dodecagon and explicitly taken the $B_\perp$ field into our least-squares fits. A similar approach has recently been adopted in [53] for their analysis of InAs NWs, where the authors hypothesized a hexagonal cross section for their NWs.

IZO1 NW, as T monotonically increases and L_φ progressively decreases, a 1D-to-2D dimensionality crossover of the WL effect first takes place around $\sim$ 7 K, where $L_\varphi(7\ \mathrm{K}) \simeq d$. As T further increases, a 2D-to-3D dimensionality crossover eventually occurs near $\sim$ 50 K, where $L_\varphi(50\ \mathrm{K}) \simeq t$. It should be noted that the existence of a relevant shell thickness of $\approx$15 nm is further supported by the EEI effect in the R–T behavior (figures 6(a) and (b)). Thus, continuously fitting the measured MR curves with the 2D WL theory up to $T > 50$ K would lead to an inconsistency of $L_\varphi^{(2D)} < t$.

Apart from the IZO1 NW, we have carried out similar MR measurements on the IZO2 NW. In this second NW, we obtain least-squares fitted average values of $d \simeq 81$ nm, $t \simeq 17$ nm, and $L_{so} \simeq 105$ nm. Figure 4(b) shows the L_φ values extracted according to the 1D, 2D, and 3D WL MR expressions, as indicated. We find that we definitely need to apply the 2D WL theory to extract acceptable values of L_φ (circles) in this NW. Those L_φ values (squares) extracted according to equation (1) are smaller than d at all T, and thus an interpretation based on the 1D WL effect is not self-consistent. On the other hand, those L_φ values (triangles) extracted according to equation (2) are larger than t at T below $\sim$ 40 K, and thus the 3D WL effect is not acceptable either for $T < 40$ K. In other words, our results suggest that the IZO2 NW lies in the 2D regime with regard to the WL effect all the way down to $T \sim 1$ K. There is no crossover to the 1D WL regime because this NW has a larger d value while it possesses a shorter L_φ, as compared with the IZO1 NW. Physically, the L_φ is shorter in the IZO2 NW because this NW is slightly more disordered than the IZO1 NW. In the opposite high T region, there is a 2D-to-3D dimensionality crossover taking place around 40 K. At 40 K, the measured MR can be fitted with both equations (2) and (3), and the extracted values are similar, with $L_\varphi(40\ \mathrm{K}) \equiv t \simeq 17$ nm. It should be noted that this t value is relatively close to that ($\simeq$15 nm) inferred for the IZO1 NW. These results suggest that this is the typical thickness of the surface conduction shell in our IZO NWs. This characteristic thickness might be a material property of the group-III metal-doped ZnO NWs [23].

3.3. Two-dimensional parallel magnetoresistance in the weak-localization effect

In this section, we intend to provide further evidence for the existence of a surface conduction shell in individual IZO NWs. If there is any quasi-2D structure leading to the 2D WL effect observed in our IZO NWs discussed thus far, measuring the MR in B applied parallel to the conduction shell should provide a complementary method for determining the thickness t of this conduction shell. The MR due to the 1D WL effect in the presence of a parallel magnetic field, $B_\parallel$, is already included in equation (1). The MR due to the 2D WL effect in the presence of a parallel $B_\parallel$ is given by [54], in terms of normalized sheet resistance $\Delta R_\square(B_\parallel)/R_\square^2(0) = (R_\square(B_\parallel) - R_\square(0))/R_\square^2(0)$,

$$\frac{\Delta R_\square(B_\parallel)}{R_\square^2(0)} = -\frac{e^2}{2\pi^2\hbar}\left[\frac{3}{2}\ln\left(1+\frac{L_2^2}{L_\parallel^2}\right) - \frac{1}{2}\ln\left(1+\frac{L_\varphi^2}{L_\parallel^2}\right)\right], \quad (4)$$

where the characteristic lengths $L_\parallel = \sqrt{3\hbar/(eB_\parallel t)}$, and $L_2 = \sqrt{\hbar/(4eB_2)}$, with the characteristic fields B_2 and B_φ being defined below equation (2).

Figures 5(a)–(c) plot the perpendicular and the parallel MR data of the IZO1 NW at three selected T values of 3 K (i.e., the 1D WL regime), 20 K (i.e., the 2D WL regime), and 50 K (i.e., the 2D-to-3D crossover regime), respectively. In each figure, the solid (dashed) curve is the theoretical prediction of the perpendicular (parallel) WL effect. We start with the low-T 1D regime. In figure 5(a), the perpendicular MR was first least-squares fitted to equation (1) with the form of $\tau_B = 12L_B^4/(D\pi d^2)$ as discussed in section 3.2, and the solid curve was plotted using the fitted parameters: $L_\varphi(3\ \mathrm{K}) = 81$ nm, $L_{so} = 140$ nm, and $d = 59$ nm. Then, we substituted this set of parameters into equation (1) but now rewrote the magnetic time in the form of $\tau_B = 8L_B^4/(Dd^2)$ to 'generate' the 1D *parallel* WL MR prediction, *without* invoking any additional adjustable parameter or performing any further least-squares fits. This procedure produced the dashed curve which is seen to well describe our measured parallel MR data. Thus, the reliability and validity of our measurement method and data analyses are justified. In fact, we could repeat this practice of using the *same* set of fitting parameters to describe both the perpendicular and the parallel MR data at a given T for all temperatures below $\approx$7 K. In figure 5(a), the magnitudes of the perpendicular MR and the parallel MR do not differ markedly, i.e., the MR is not significantly anisotropic, because L_φ (3 K) is not considerably longer than d in this NW.[6]

At $T > 7$ K, our measured perpendicular MR data and the parallel MR data at a given T can *no longer* be simultaneously described by equation (1) with the same set of adjustable parameters. Therefore, we have turned to the 2D forms of the WL theory. In this procedure, if we already know the L_φ and L_{so} values from the analyses of the perpendicular MR data at a given T as discussed in section 3.2, the conduction shell thickness t (which enters $L_\parallel$) will be the *sole* adjustable parameter left in equation (4). Figures 5(b) and (c) clearly show that our perpendicular MR data and parallel MR data can be simultaneously described by equation (3) (solid curves) and equation (4) (dashed curves), respectively. From this approach, our extracted t value according to equation (4) is $\simeq$15 nm at both temperatures, firmly confirming the above deduced thickness. In fact, by repeating for several T values in the 2D WL regime, we obtain average values of $t \simeq 15 \pm 2$ nm for the IZO1 NW and $t \simeq 17 \pm 3$ nm for the IZO2 NW (table 3).

Figure 5(d) shows a plot of the perpendicular MR data (open squares) and the parallel MR data (closed circles) as a function of B for the IZO2 NW at 70 K. One sees that the perpendicular MR and the parallel MR collapse, explicitly

[6] We note that a minute misalignment of the NW axis with respect to the $B_\parallel$ field would cause an extra contribution from the perpendicular component of $B_\parallel$ to the measured parallel MR data. In this experiment, we estimate that there could be a small misalignment of <5°. Since the WL MR curves of the IZO NWs are not dramatically anisotropic, any possible tiny erroneous contribution from the perpendicular component of the $B_\parallel$ field should thus be insignificant in this work.

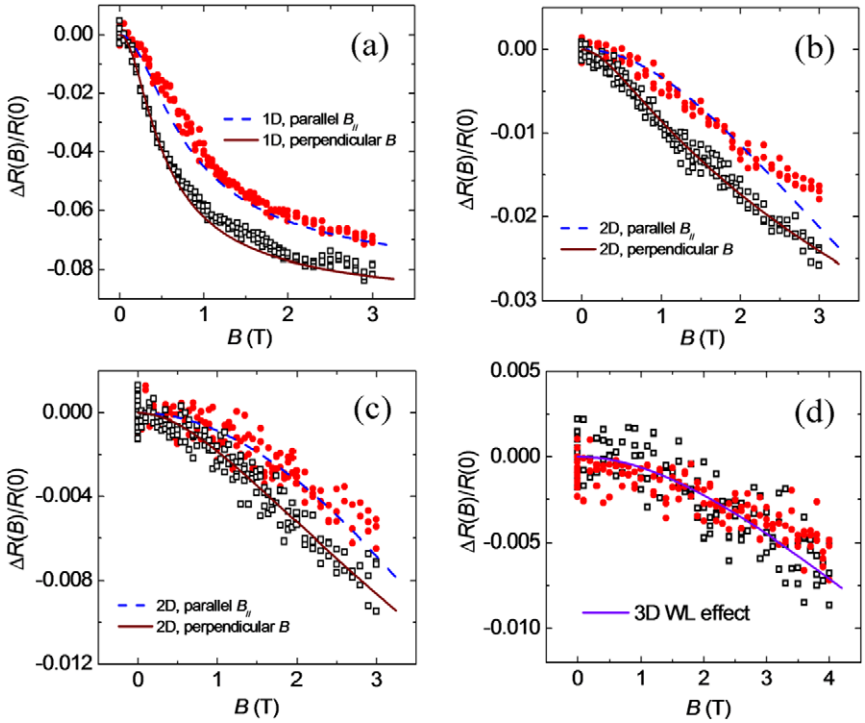

Figure 5. Normalized MR, $\Delta R(B)/R(0) = (R(B) - R(0))/R(0)$, as a function of magnetic field for the IZO1 NW at (a) 3.0 K, (b) 20 K, and (c) 50 K. (d) $\Delta R(B)/R(0)$ as a function of magnetic field of the IZO2 NW at 70 K. In each figure, open squares (closed circles) are the perpendicular (parallel) MR data. The solid (dashed) curves are the theoretical predictions of the perpendicular (parallel) WL effects. The solid curve in (d) is a least-squares fit to equation (2) with $L_\varphi = 11$ nm.

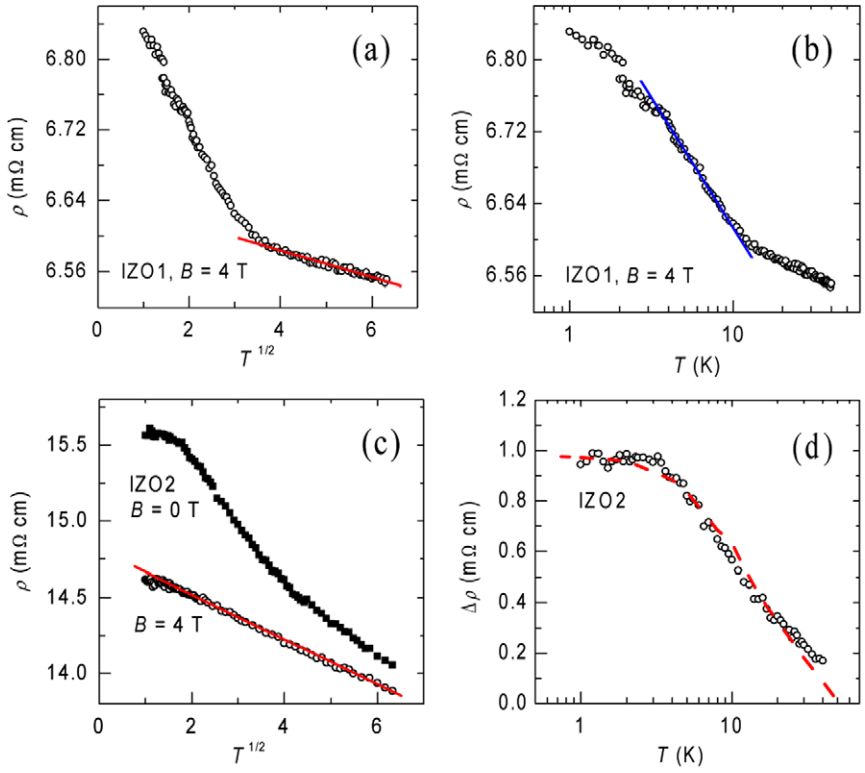

Figure 6. Resistivity of the IZO1 NW measured in a perpendicular B field of 4 T as a function of (a) the square root of temperature, and (b) the logarithm of temperature. (c) Resistivity as a functions of the square root of temperature for the IZO2 NW measured in $B = 0$ and in perpendicular $B = 4$ T, as indicated. (d) A plot of the difference in resistivity from (c), $\Delta\rho = \rho(B = 0) - \rho(B = 4\ \text{T})$, as a function of the logarithm of temperature. The straight solid line in (b) is a least-squares fit to equation (5), and the straight solid lines in (a) and (c) are least-squares fits to equation (6). The dashed curve in (d) is the theoretical prediction of equation (7).

Table 3. Least-squares fitted parameters for IZO NWs. $A_{ee}^{(1D)}$, $A_{ee}^{(2D)}$, and $A_{ee}^{(3D)}$ are the electron–electron scattering strengths in the 1D, 2D, and 3D regimes, respectively. τ_0 is the electron dephasing time as $T \to 0$ K, τ_{so} is the spin–orbit scattering time, d is the effective NW diameter, w is the perimeter of the dodecagon assumed in the least-squares fits to equation (3), and t is the outer conduction shell thickness.

Sample	$A_{ee}^{(1D)}$ $K^{-2/3}\,s^{-1}$	$A_{ee}^{(2D)}$ $K^{-1}\,s^{-1}$	$A_{ee}^{(3D)}$ $K^{-3/2}\,s^{-1}$	τ_0 (ps)	τ_{so} (ps)	d (nm)	w (nm)	t (nm)
IZO1	1.6×10^{10}	1.1×10^{10}	2.3×10^{9}	~67	54	59	159	15 ± 2
IZO2	—	9.0×10^{9}	2.2×10^{9}	~40	47	81	235	17 ± 3

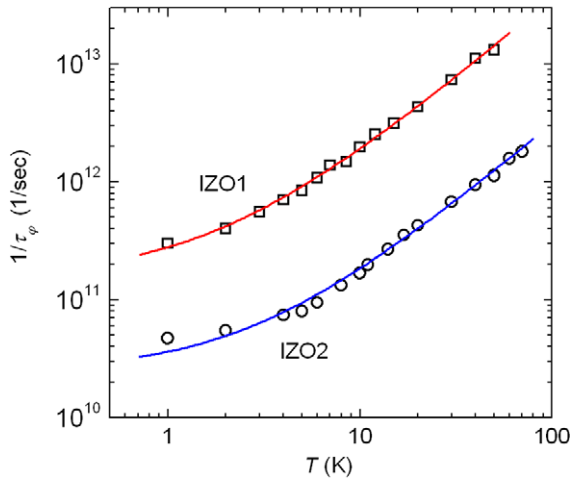

Figure 7. Electron dephasing rate τ_φ^{-1} as a function of temperature for the IZO1 and IZO2 NWs, as indicated. The solid curves are the theoretical predictions of equation (8). For clarity, the data of the IZO1 NW have been shifted up by multiplying by a factor of 10. Note that the two data points at 1 K might be subject to slight electron heating.

illustrating a 3D behavior. Indeed, at such a high T value, L_φ must be very short. According to equation (2) (the solid curve), we obtain a least-squares fitted value of $L_\varphi(70\ \text{K}) \simeq 11$ nm.

3.3.1. Self-purification mechanisms preventing doping of semiconductor nanostructures. It should be of crucial importance to point out that, from the Hall effect and secondary-ion mass spectroscopy measurements, Look *et al* [23] have recently inferred that the group-III metal impurities could readily diffuse into the surfaces of any ZnO wafers for a distance of ≈14 nm. Remarkably, this value independently inferred from entirely distinct physical properties is in close agreement with our extracted t value (≃15–17 nm). The underlying physics for this consistency is highly meaningful. Recently, based on energetic arguments, Dalpian and Chelikowsky [30] have theoretically shown that the 'self-purification' mechanisms would perniciously prevent doping of semiconductor nanostructures, causing dopants to segregate to surfaces. This theoretical finding provides a natural explanation for our experimental observation of the 'core–shell-like structure' in IZO NWs. This very issue concerning the materials property and the doping behavior of semiconductors at the nanoscale deserves detailed studies before any nanoelectronic devices could be possibly implemented [55].

3.3.2. The absence of Altshuler–Aronov–Spivak (AAS) oscillations. It may be conjectured that a convincing experimental proof of the existence of an outer conduction shell would be an observation of the AAS oscillations at low temperatures [56]. AAS had theoretically predicted that the resistance of a weakly disordered cylindrical conductor would oscillate in sweeping $B_\parallel$ fields with a period of $h/2e$. We have checked this predicted phenomenon in this study, but did not observe any signature of such a kind of oscillation. This is expected, because a conduction shell as thick as ≃15–17 nm in our IZO NWs would strongly suppress the amplitudes of the AAS oscillations, making them more than one order of magnitude smaller than the parallel MR in the WL effect[7]. Moreover, the AAS oscillations should be further damped due to any inhomogeneities in the conduction shell radius and thickness [58], which very likely exist in our NWs.

4. Dimensionality crossover in the electron–electron interaction effect

In this section, we concentrate on the $R(T)$ data due to the EEI effect to provide further justification for the existence of a core–shell-like structure in IZO NWs. In addition to the WL effect, the many-body EEI effect also results in a resistance rise with decreasing T in a weakly disordered conductor [24–26]. The EEI effect induced correction in 2D is given by [26, 50], in terms of the normalized sheet resistance $\Delta R_\square(T)/R_\square(T_0) = (R_\square(T) - R_\square(T_0))/R_\square(T_0)$,

$$\frac{\Delta R_\square(T)}{R_\square(T_0)} = -\frac{e^2}{2\pi^2\hbar}\left(1 - \frac{3}{4}\tilde{F}\right)R_\square \ln\left(\frac{T}{T_0}\right), \qquad (5)$$

where T_0 is an arbitrary reference temperature. $\tilde{F}$ is an electron screening factor averaged over the Fermi surface, whose value lies approximately between 0 and 1 [26, 59]. The EEI effect induced correction in 3D is given by [26, 60], in terms of the normalized resistivity $\Delta\rho(T)/\rho(T_0) = (\rho(T) - \rho(T_0))/\rho(T_0)$,

$$\frac{\Delta\rho(T)}{\rho(T_0)} = -\frac{0.915e^2}{4\pi^2\hbar}\left(\frac{4}{3} - \frac{3}{2}\tilde{F}\right)\rho\sqrt{\frac{k_B}{\hbar D}}\left(\sqrt{T} - \sqrt{T_0}\right). \qquad (6)$$

In the comparison of the theoretical prediction of either equation (5) or equation (6) with experiment, $\tilde{F}$ is the

[7] We notice that signatures of the AAS oscillations have recently been observed in radial core–shell In_2O_3/InO_x heterostructure NWs [57]. The authors found that the electrical current flowed dominantly through the core–shell interface, but not through the whole shell region. A very thin interface layer of sub-nanometer scale could sustain the AAS oscillations.

only adjustable parameter. The characteristic length scale controlling the sample dimensionality in the EEI effect is the thermal diffusion length $L_T = \sqrt{D\hbar/k_B T}$. Note that the EEI effect in different sample dimensionalities results in distinct T dependences of the resistance rise at low temperatures[8]. The WL effect induced corrections to the residual resistance at low T can be readily suppressed by applying a moderately high B field [24–26]. Therefore, one may measure $R(T)$ in an applied field to focus on the EEI term alone.

We start with our discussion of the IZO2 NW. Figure 6(c) shows the resistivity of the IZO2 NW as a function of $\sqrt{T}$ in both $B = 0$ and in a perpendicular $B = 4$ T, as indicated. Clearly, the 4 T data illustrate a robust linear dependence between ∼3 and 40 K. Such a $-\sqrt{T}$ temperature dependence manifests the 3D EEI effect in this wide T interval. By comparing with the prediction of equation (6), we obtained a value $\tilde{F} \simeq 0.42$. This magnitude of $\tilde{F}$ is in line with that found in typical doped semiconductors, such as Si:B [61]. On the other hand, in $B = 0$, the T dependence of ρ is somewhat more complicated, because both the WL and the EEI effects now contribute to the total resistivity rise. Using $D = 2.2$ cm^2 s^{-1} (table 2), we estimate $L_T(5\text{ K}) \simeq 18$ nm. This length scale is basically the conduction shell thickness inferred from the WL MR studies (section 3). That is, the 3D EEI effect on the resistivity rise is expected to persist from intermediately high T down to ∼5 K in this particular NW. This prediction is in good accord with the observation depicted in figure 6(c).

Figure 6(d) plots the variation of the difference in the measured resistivity, $\Delta\rho = \rho(B = 0) - \rho\ (B = 4\text{ T})$, with temperature of the IZO2 NW whose resistivities are shown in figure 6(c). This figure indicates an approximate $\ln T$ temperature dependence of $\Delta\rho$ between ∼3 and ∼40 K. This observation is meaningful. Indeed, this $\Delta\rho$ can be identified as originating from the 2D WL effect, which is theoretically predicted to be given by [26], in terms of the normalized sheet resistance,

$$\frac{\Delta R_\square(T)}{R_\square(T_0)} = \frac{e^2}{4\pi^2\hbar} R_\square \left\{ \ln\left[\frac{B_\varphi(T)}{B_\varphi(T_0)}\right] - 3\ln\left[\frac{B_2(T)}{B_2(T_0)}\right]\right\}, \quad (7)$$

where T_0 is an arbitrary reference temperature, and B_2 and B_φ are defined below equation (2). Writing $\rho = tR_\square$ and substituting the fitted values of L_φ and L_{so} from our MR data analyses described in section 3 into equation (7), we obtain the dashed curve shown in figure 6(d), which is seen to satisfactorily describe the experimental $\Delta\rho$. This result strongly confirms our scenario of the quantum-interference transport through a surface layer in single IZO NWs. Recall that the 2D WL MR effect in the IZO2 NW has been observed in the same T interval of 1–40 K (section 3.2). Below about 3 K, $\Delta\rho$ tends to saturate to a constant value, because τ_φ becomes very weakly dependent on T, as shown in figure 4(b).

We turn to the IZO1 NW. For simplicity, we shall present and discuss only the $\rho(T)$ data measured in a perpendicular $B = 4$ T. Figure 6(a) shows that the $\rho \propto -\sqrt{T}$ law holds between ∼14 and 40 K. By comparing with equation (6), we obtained a value of $\tilde{F} \simeq 0.61$. In contrast to the case of the IZO2 NW, a change in the T dependence to the 2D $R_\square \propto -\ln T$ law is seen between ∼3.6 and ∼11 K in this NW; see figure 6(b). By writing $R_\square = \rho/t$ and comparing with the prediction of equation (5), we obtained a value $\tilde{F} \simeq 0.51$. This value is reasonably in line with that inferred above from the high-T 3D regime. Thus, a dimensionality crossover with regard to the EEI effect does occur in the ∼11–14 K temperature window in this particular NW. In fact, using $D = 3.6$ cm^2 s^{-1} (table 2), we estimate $L_T(11\text{ K}) = 16$ nm. This value is very close to the conduction shell thickness $t \simeq 15$ nm inferred from the WL MR studies discussed in section 3. In other words, at $T \gtrsim 11$ K, $L_T \lesssim t$ and the EEI effect is 3D (figure 6(a)), while at $T \lesssim 11$ K, $L_T \gtrsim t$ and the EEI effect is 2D (figure 6(b)). In short, the observations of a 2D-to-3D dimensionality crossover in both the EEI effect and the WL effect strongly substantiate the existence of an outer conduction shell of thickness t in IZO NWs.

Finally, it may be readily estimated that the thermal lengths $L_T(T) = 52/\sqrt{T}$ nm in the IZO1 NW and $41/\sqrt{T}$ nm in the IZO2 NW. These lengths are relatively short, as compared with d. Thus, a dimensionality crossover of the EEI effect from the 2D to the 1D regime is not seen in this experiment. Table 1 summarizes the various T intervals over which different dimensionalities in the WL and the EEI effects are observed in this work.

5. Electron dephasing time

In this section, we analyze the T dependence of τ_φ^{-1} to study the electron dephasing processes in IZO NWs. Recall that, for a given IZO NW, the 'correct' τ_φ^{-1} values in different T regions are those extracted according to the appropriate WL MR expressions in different dimensionalities. Figure 7 plots our extracted τ_φ^{-1} as a function of T for the IZO1 and IZO2 NWs, as indicated. In this figure, the τ_φ^{-1} values of the IZO1 NW are a combination of those extracted according to the 1D WL form (equation (1)) between 1 and 8.5 K and those extracted according to the 2D WL form (equation (3)) between 7 and 50 K. The τ_φ^{-1} values of the IZO2 NW are a combination of those extracted according to the 2D WL form (equation (3)) between 1 and 40 K and those extracted according to the 3D WL form (equation (2)) between 40 and 70 K.

The physical meaning of τ_φ^{-1} is examined in the following. The total electron dephasing rate in a weakly disordered degenerate semiconductor can be written as [35]

$$\frac{1}{\tau_\varphi(T)} = \frac{1}{\tau_0} + \frac{1}{\tau_{ee}^N(T)} + \frac{1}{\tau_{in}(T)}, \quad (8)$$

where τ_0 is a constant or a very weakly T dependent quantity, whose origins (paramagnetic impurity scattering, dynamical structural defects, etc) have been a subject of elaborate investigations in the past three decades [41, 62–64]. The quasi-elastic (i.e., small-energy-transfer) Nyquist electron–electron (e–e) relaxation rate, $(\tau_{ee}^N)^{-1}$, in low-dimensional disordered conductors is known to dominate τ_φ^{-1}

[8] Apart from equations (5) and (6), the EEI effect causes a $-1/\sqrt{T}$ temperature dependence of the resistance rise in 1D, which is not seen in this study.

in an appreciable T interval. In the following analyses, we use the standard expression $(\tau_{ee}^{N})^{-1} = A_{ee}T^{p}$, where $p = 2/3$ and 1 for 1D and 2D samples, respectively [26, 35, 65]. Note that, as T increases, the exponent of temperature p in $(\tau_{ee}^{N})^{-1}$ is expected to change as the sample dimensionality changes in our IZO NWs. The third term, τ_{in}^{-1}, on the right-hand side of equation (8) denotes any additional inelastic scattering mechanism(s) that might play a role in the dephasing process at sufficiently high T.

Before comparing our experimental τ_{φ}^{-1} data with equation (8), we first would like to comment on the electron–phonon (e–ph) relaxation process. In disordered metals, the e–ph scattering is often significant at a few kelvin and higher. One may then safely identify the τ_{in}^{-1} term in equation (8) as the e–ph scattering rate τ_{e-ph}^{-1} [66], in either the diffusive limit [67, 68] or the quasi-ballistic limit [69], depending on the experimental conditions. However, the carrier concentrations $n \sim 1 \times 10^{19}$ cm^{-3} (table 2) in our IZO NWs, which are three to four orders of magnitude lower than those in typical metals [70]. Theoretical evaluations show that, at such carrier concentrations, the deformation potential still has a metallic nature, but substantially decreases due to the low concentration. The corresponding e–ph coupling constant (the constant β in [66, 69]) is found to be proportional to n. Therefore, the e–ph relaxation must be *negligible* in this work[9]. In contrast, it should be pointed out that the e–e scattering in the IZO material relative to that in typical metals is enhanced, owing to the smaller E_F value and the larger ρ ($R_{\square}$) value in IZO NWs.

In 3D, it is established that the e–e scattering is determined by the large-energy-transfer processes. In the clean limit, the theory [26, 35] predicts $(\tau_{ee}^{-1})_{clean} = \pi(k_B T)^2/(8\hbar E_F)$. Substituting the E_F values of our IZO NWs into this expression, we estimate this scattering rate to be $\approx 4 \times 10^7 T^2$ s^{-1} ($\approx 8 \times 10^7 T^2$ s^{-1}) in the IZO1 (IZO2) NW. Even at a moderately high T of 40 K, this scattering rate is more than (about) one order of magnitude smaller than the experimental τ_{φ}^{-1} value in the IZO1 (IZO2) NW. Therefore, this clean-limit e–e scattering process can be ruled out in the present study. In the dirty limit, the large-energy-transfer e–e scattering rate is modified to be $\tau_{ee}^{-1} = A_{ee}^{(3D,th)}T^{3/2}$, with the coupling strength given by [26, 35, 65]

$$A_{ee}^{(3D,th)} = \frac{\sqrt{3}}{2\hbar\sqrt{E_F}}\left(\frac{k_B}{k_F \ell}\right)^{3/2}. \quad (9)$$

This scattering rate is relevant to our experiment at high T values where our NWs enter the 3D WL regime.

[9] Due to this relatively weak e–ph coupling strength, one needs to be extremely careful about any possible electron overheating effect on the electrical-transport measurements at low T. On the other hand, this relatively weak e–ph coupling strength (partly) explains the reason why the quantum-interference WL MR can persist to $T \gtrsim 70$ K in IZO NWs [72]. We also would like to note that, in a recent study of ZnO nanoplates with relatively low n values, Likovich *et al* [37] have reported a $\tau_{in}^{-1} \propto T^3$ law between 2 and 10 K. They also found that the τ_{in} magnitude increased with increasing n. More precisely, they reported that τ_{in}(1.9 K) increased from $\sim$ 3.0 to $\sim$5.7 ns as n increased from 1.3×10^{17} to 7.4×10^{17} cm^{-3}. Although the authors had attributed their inelastic scattering rate to τ_{e-ph}^{-1}, these results seem to be hard to reconcile with the current understanding of the e–ph relaxation process in degenerate semiconductors.

Since the dimensionality crossover in the WL effect is less complex in the IZO2 NW, we first analyze the τ_{φ}^{-1} data in this sample. In this NW, there is a single 2D-to-3D crossover in the wide T interval of 1–70 K. Therefore, we may rewrite equation (8) in the following form: $\tau_{\varphi}^{-1} = \tau_0^{-1} + A_{ee}^{(2D)}T + A_{ee}^{(3D)}T^{3/2}$, where $A_{ee}^{(2D)}$ and $A_{ee}^{(3D)}$ denote the e–e scattering strength in the 2D and 3D regimes, respectively. (One may identify $A_{ee}^{(3D)}T^{3/2}$ as the τ_{in}^{-1} term in equation (8).) By least-squares fitting this expression to the experimental data (see figure 7), we obtain $A_{ee}^{(2D)} \simeq 9.0 \times 10^9$ K^{-1} s^{-1} and $A_{ee}^{(3D)} \simeq 2.2 \times 10^9$ K$^{-3/2}$ s^{-1}. Theoretically, the Nyquist e–e scattering strength in 2D is given by [26, 35, 65]

$$A_{ee}^{(2D,th)} = \frac{e^2 k_B}{2\pi\hbar^2} R_{\square} \ln\left(\frac{\pi\hbar}{e^2 R_{\square}}\right). \quad (10)$$

Substituting our experimental value of $R_{\square}$ into equation (10), we obtain $A_{ee}^{(2D,th)} = 1.8 \times 10^{10}$ K^{-1} s^{-1}. Also, substituting our experimental values of E_F and k_F into equation (9), we obtain $A_{ee}^{(3D,th)} = 2.7 \times 10^9$ K$^{-3/2}$ s^{-1}. These values are in good agreement with the experimental values. Therefore, we can clearly identify the e–e scattering as the dominating dephasing process in the IZO2 NW. We notice that our $A_{ee}^{(2D)}$ value is on the same order of magnitude as that found in the ZnO surface wells [71].

Our fitted τ_0 value for the IZO2 NW is listed in table 3. It should be noted that the fitted τ_0 value is only approximate, because we have not extensively measured the MR curves at subkelvin T values to unambiguously extract $\tau_0 = \tau_{\varphi}$ ($T \to 0$ K). We also note that, at our lowest measurement temperature of 1 K, the electrons in the NW might have been slightly overheated.

The electron dephasing processes in the IZO1 NW is somewhat more complicated and requires a more detailed examination. Because both 1D-to-2D and 2D-to-3D dimensionality crossovers in the WL effect are observed, we first write equation (8) in the form $\tau_{\varphi}^{-1} = \tau_0^{-1} + A_{ee}^{(2D)}T + A_{ee}^{(3D)}T^{3/2}$ to extract the values of $A_{ee}^{(2D)}$ and $A_{ee}^{(3D)}$ using data in the $T \simeq$ 10–50 K interval. Then, we write equation (8) in the form $\tau_{\varphi}^{-1} = \tau_0^{-1} + A_{ee}^{(1D)}T^{2/3}$ to extract the values of τ_0^{-1} and $A_{ee}^{(1D)}$ using data in the $T \simeq$ 2–10 K interval. Our fitted result in figure 7 is obtained with the following values: $A_{ee}^{(1D)} \approx 1.6 \times 10^{10}$ K$^{-2/3}$ s^{-1}, $A_{ee}^{(2D)} \approx 1.1 \times 10^{10}$ K^{-1} s^{-1}, and $A_{ee}^{(3D)} \approx 2.3 \times 10^9$ K$^{-3/2}$ s^{-1}. Substituting our experimental value of $R_{\square}$ into equation (10), we obtain $A_{ee}^{(2D,th)} = 2.4 \times 10^{10}$ K^{-1} s^{-1}. Substituting our experimental values of E_F and k_F into equation (9), we obtain $A_{ee}^{(3D,th)} = 9.8 \times 10^8$ K$^{-3/2}$ s^{-1}. Our experimental values are within a factor of $\approx$2 of the 2D and 3D theoretical values, and thus are satisfactory.

In 1D, the Nyquist e–e scattering strength is theoretically predicted to be [5, 26, 65]

$$A_{ee}^{(1D,th)} = \left(\frac{e^2\sqrt{D}Rk_B}{2\sqrt{2}\hbar^2 L}\right)^{2/3}. \quad (11)$$

Substituting our measured NW resistance R, length L, and diffusion constant D into equation (11), we obtain $A_{ee}^{(1D,th)} \approx$

2.5×10^{10} $K^{-2/3}$ s^{-1}. This value is about 50% higher than our experimental value, and hence our result is well acceptable[10].

6. Conclusion

We have measured the temperature dependence of resistance as well as the magnetic field dependence of magnetoresistance in two indium-doped ZnO nanowires. The doped NWs reveal overall metallic-transport properties characteristic of disordered conductors. Our results lead to our proposition of a core–shell-like structure in individual IZO NWs, with the outer shell of thickness $\simeq$15–17 nm being responsible for the observed quantum-interference WL and EEI effects. As a consequence, 1D-to-2D and 2D-to-3D dimensionality crossovers in the WL effect are evident as the temperature gradually increases from 1 to 70 K. A 2D-to-3D dimensionality crossover in the EEI effect has also been observed. A crossover to the 1D EEI effect is not seen, because the thermal diffusion length $L_T(T)$ is relatively short, as compared with the effective NW diameter d. These observations reveal the complex and rich nature of the charge-transport processes in group-III metal-doped ZnO NWs. In addition, we have explained the inelastic electron dephasing times. It should be emphasized that our experimental observation of a core–shell-like structure in IZO NWs is in good accord with the current theoretical understanding for impurity doping of semiconductor nanostructures. This result could have significant bearing on the potential implementation of nanoelectronic devices.

Acknowledgments

This work was supported by the Taiwan National Science Council through grant No NSC 100-2120-M-009-008 and by the MOE ATU Program (JJL). Research by JGL was supported by NSF.

References

[1] Nazarov Y V and Blanter Y M 2009 *Quantum Transport: Introduction to Nanoscience* (Cambridge: Cambridge University Press)
[2] Chiquito A J, Lanfredi A J C, de Oliveira R F M, Pozzi L P and Leite E R 2007 *Nano Lett.* **7** 1439
[3] Lin Y H, Sun Y C, Jian W B, Chang H M, Huang Y S and Lin J J 2008 *Nanotechnology* **19** 045711
[4] Chiu S P, Chung H F, Lin Y H, Kai J J, Chen F R and Lin J J 2009 *Nanotechnology* **20** 105203
[5] Hsu Y W, Chiu S P, Lien A S and Lin J J 2010 *Phys. Rev.* B **82** 195429

[10] We comment that, in the recent study of Ge/Si core–shell NWs by Hau *et al* [13], the authors had carried out two-probe MR measurements on a single NW over a very wide T range of 0.4–150 K. They had applied the 1D WL MR form to this wide T interval and in applied perpendicular B fields up to as high as 8 T. Hau *et al* then interpreted their extracted τ_φ^{-1} in terms of equation (11) alone. It is puzzling why the e–e scattering with large-energy transfer and other inelastic electron scattering processes did not play any role even up to such a high T of 150 K. It is also not clear if any dimensionality crossover in the WL effect had taken place in the sample. These issues need further clarification.

[6] Yang P Y, Wang L Y, Hsu Y W and Lin J J 2012 *Phys. Rev.* B **85** 085423
[7] Tatara G, Kohno H and Shibata J 2008 *Phys. Rep.* **468** 213
[8] Rueß F J, Weber B, Goh K E J, Klochan O, Hamilton A R and Simmons M Y 2007 *Phys. Rev.* B **76** 085403
[9] Chiu S P, Lin Y H and Lin J J 2009 *Nanotechnology* **20** 015203
[10] Tsai L T, Chiu S P, Lu J G and Lin J J 2010 *Nanotechnology* **21** 145202
[11] Petersen G, Hernández S E, Calarco R, Demarina N and Schapers Th 2009 *Phys. Rev.* B **80** 125321
[12] Liang D, Du J and Gao X P A 2010 *Phys. Rev.* B **81** 153304
[13] Hao X J, Tu T, Cao G, Zhou C, Li H O, Guo G C, Fung W Y, Ji Z, Guo G P and Lu W 2010 *Nano Lett.* **10** 2956
[14] Xu X, Irvine A C, Yang Y, Zhang X and Williams D A 2010 *Phys. Rev.* B **82** 195309
[15] Hernández S E, Akabori M, Sladek K, Volk Ch, Alagha S, Hardtdegen H, Pala M G, Demarina N, Grützmacher D and Schäpers Th 2010 *Phys. Rev.* B **82** 235303
[16] Zeng Y J, Pereira L M C, Menghini M, Temst K, Vantomme A, Locquet J-P and Van Haesendonck C 2012 *Nano Lett.* **12** 666
[17] Arutyunov K Yu, Golubev D S and Zaikin A D 2008 *Phys. Rep.* **464** 1
[18] Özgür Ü, Alivov Ya I, Liu C, Teke A, Reshchikov M A, Doğan S, Avrutin V, Cho S-J and Morkoc H 2005 *J. Appl. Phys.* **98** 041301
[19] Wang Z L 2008 *ACS Nano* **2** 1987
[20] Liu K W, Sakurai M and Aono M 2010 *J. Appl. Phys.* **108** 043516
[21] Ahn B D, Oh S H, Kim H J, Jung M H and Ko Y G 2007 *Appl. Phys. Lett.* **91** 252109
[22] Thompson R S, Li D, Witte C M and Lu J G 2009 *Nano Lett.* **9** 3991
[23] Look D C, Claflin B and Smith H E 2008 *Appl. Phys. Lett.* **92** 122108
[24] Bergmann G 1984 *Phys. Rep.* **107** 1
[25] Bergmann G 2010 *Int. J. Mod. Phys.* B **24** 2015
[26] Altshuler B L and Aronov A G 1985 *Electron–Electron Interactions in Disordered Systems* ed A L Efros and M Pollak (Amsterdam: Elsevier)
[27] Schlenker E, Bakin A, Weimann T, Hinze P, Weber D H, Gölzhäuser A, Wehmann H-H and Waag A 2008 *Nanotechnology* **19** 365707
[28] Allen M W, Swartz C H, Myers T H, Veal T D, McConville C F and Durbin S M 2010 *Phys. Rev.* B **81** 075211
[29] Hu Y, Liu Y, Li W, Gao M, Liang X, Li Q and Peng L M 2009 *Adv. Funct. Mater.* **19** 2380
[30] Dalpian G M and Chelikowsky J R 2006 *Phys. Rev. Lett.* **96** 226802
[31] Ellmer K 2001 *J. Phys. D: Appl. Phys.* **34** 3097
[32] Hutson A R 1957 *Phys. Rev.* **108** 222
[33] Baer W S 1967 *Phys. Rev.* **154** 785
[34] Lien C C, Wu C Y, Li Z Q and Lin J J 2011 *J. Appl. Phys.* **110** 063706
[35] Lin J J and Bird J P 2002 *J. Phys.: Condens. Matter* **14** R501
[36] Mani R G, von Klitzing K and Ploog K 1993 *Phys. Rev.* B **48** 4571
[37] Likovich E M, Russell K J, Petersen E W and Narayanamurti V 2009 *Phys. Rev.* B **80** 245318
[38] Andrearczyk T, Jaroszyński J, Grabecki G, Dietl T, Fukumura T and Kawasaki M 2005 *Phys. Rev.* B **72** 121309(R)
[39] Harmon N J, Putikka W O and Joynt R 2009 *Phys. Rev.* B **79** 115204
[40] Altshuler B L and Aronov A G 1981 *JETP Lett.* **33** 499
[41] Pierre F, Gougam A B, Anthore A, Pothier H, Esteve D and Birge N O 2003 *Phys. Rev.* B **68** 085413

[42] Shalish I, Temkin H and Narayanamurti V 2004 *Phys. Rev.* B **69** 245401
[43] Grinshpan Y, Nitzan M and Goldstein Y 1979 *Phys. Rev.* B **19** 1098
[44] Göpel W and Lampe U 1980 *Phys. Rev.* B **22** 6447
[45] Fukuyama H and Hoshino K 1981 *J. Phys. Soc. Japan* **50** 2131
[46] Wu C Y and Lin J J 1994 *Phys. Rev.* B **50** 385
[47] Reynolds D C, Litton C W and Collins T C 1965 *Phys. Rev.* **140** A1726
[48] Baxter D V, Richter R, Trudeau M L, Cochrane R W and Strom-Olsen J O 1989 *J. Physique* **50** 1673
[49] Hikami S, Larkin A I and Nagaoka Y 1980 *Prog. Theor. Phys.* **63** 707
[50] Lin J J and Giordano N 1987 *Phys. Rev.* B **35** 545
[51] Langer L, Bayot V, Grivei E, Issi J-P, Heremans J P, Olk C H, Stockman L, Van Haesendonck C and Bruynseraede Y 1996 *Phys. Rev. Lett.* **76** 479
[52] Tarkiainen R, Ahlskog M, Zyuzin A, Hakonen P and Paalanen M 2004 *Phys. Rev.* B **69** 033402
[53] Blömers Ch, Lepsa M I, Luysberg M, Grutzmacher D, Lüth H and Schäpers Th 2011 *Nano Lett.* **11** 3550
[54] Giordano N and Pennington M A 1993 *Phys. Rev.* B **47** 9693
[55] Klamchuen A, Yanagida T, Kanai M, Nagashima K, Oka K, Seki S, Suzuki M, Hidaka Y, Kai S and Kawai T 2011 *Appl. Phys. Lett.* **98** 053107
[56] Altshuler B L, Aronov A G, Spivak B Z, Sharvin D Yu and Sharvin Yu V 1982 *JETP Lett.* **35** 588
[57] Jung M *et al* 2008 *Nano Lett.* **8** 3189
[58] Aronov A G and Sharvin Yu V 1987 *Rev. Mod. Phys.* **59** 755
[59] Jian W B, Wu C Y, Chuang Y L and Lin J J 1996 *Phys. Rev.* B **54** 4289
[60] Lin J J and Wu C Y 1993 *Phys. Rev.* B **48** 5021
[61] Dai P, Zhang Y and Sarachik M P 1992 *Phys. Rev.* B **45** 3984
[62] Lin J J and Giordano N 1987 *Phys. Rev.* B **35** 1071
[63] Mohanty P, Jariwala E M Q and Webb R A 1997 *Phys. Rev. Lett.* **78** 3366
[64] Huang S M, Lee T C, Akimoto H, Kono K and Lin J J 2007 *Phys. Rev. Lett.* **99** 046601
[65] Altshuler B L, Aronov A G and Khmelnitsky D E 1982 *J. Phys. C: Solid State Phys.* **15** 7367
[66] Sergeev A and Mitin V 2000 *Phys. Rev.* B **61** 6041
[67] Lin J J and Wu C Y 1995 *Europhys. Lett.* **29** 141
[68] Zhong Y L and Lin J J 1998 *Phys. Rev. Lett.* **80** 588
[69] Zhong Y L, Sergeev A, Chen C D and Lin J J 2010 *Phys. Rev. Lett.* **104** 206803
[70] Kittel C 2005 *Introduction to Solid State Physics* (New York: Wiley)
[71] Goldenblum A, Bogatu V, Stoica T, Goldstein Y and Many A 1999 *Phys. Rev.* B **60** 5832
[72] Wu C Y, Lin B T, Zhang Y J, Li Z Q and Lin J J 2012 *Phys. Rev.* B **85** 104204